Earth and Planetary Science Letters 593 (2022) 117688

Contents lists available at ScienceDirect

Earth and Planetary Science Letters

www.elsevier.com/locate/epsl

3D transdimensional seismic tomography of the inner core

Henry Brett [a,*], Rhys Hawkins [a], Lauren Waszek [b,c], Karen Lythgoe [d], Arwen Deuss [a]

[a] Utrecht University, Department of Geosciences, Netherlands
[b] Physical Sciences, James Cook University, Australia
[c] Department of Physics, New Mexico State University, United States of America
[d] Earth Observatory of Singapore, Nanyang Technological University, Singapore

ARTICLE INFO

Article history:
Received 27 November 2021
Received in revised form 15 June 2022
Accepted 17 June 2022
Available online 6 July 2022
Editor: H. Thybo

Keywords:
inner core
seismology
anisotropy

ABSTRACT

Body wave observations of the Earth's inner core show that it contains strong seismic heterogeneity, both laterally and radially. Models of inner core structure generated using body wave data are often limited by their parameterisation. Thus, it is difficult to determine whether features such as anisotropic hemispheres or an innermost inner core truly exist with their simple shapes, or result only from the chosen parameterisation and are in fact more complex features. To overcome this limitation, we conduct seismic tomography using transdimensional Markov Chain Monte Carlo on a high quality dataset of 5296 differential and 2344 absolute P-wave travel times. In a transdimensional approach, the data defines the model space parameterisation, providing us with both the mean value of each model parameter and its probability distribution, allowing us to identify well versus poorly constrained regions. We robustly recover many first order observations found in previous studies without the imposition of a priori fixed geometry including an isotropic top layer (with anisotropy less than 1%) which is between 60 and 170 km thick, and separated into hemispheres with a slow west and a faster east. Strong anisotropy (with a maximum of 7.2%) is found mainly in the west, with much weaker anisotropy in the east. We observe for the first time that the western anisotropic zone is largely confined to the northern hemisphere, a property which would not be recognised in models assuming a simple hemispherical parameterisation. We further find that the inner most inner core, in which the slowest anisotropic velocity direction is tilted relative to Earth's axis of rotation ($\zeta = 55° \pm 16°$), is offset by 400 km from the centre of the inner core and is restricted to the eastern hemisphere. We propose that this anomalous anisotropy might indicate the presence of a different phase of iron (either bcc or fcc) compared to the rest of the inner core (hcp).

1. Introduction

The Earth's inner core was first discovered by Lehmann (1936) through analysis of the P-wave outer core shadow zone. It is a solid sphere composed of an iron and nickel alloy with a radius of approximately 1217.5 km. Despite its remote location, the inner core has an essential role in the origin of many dynamic processes; in particular, its solidification and the resulting release of latent heat, drive convection in the outer core and thus sustain Earth's magnetic field. This latent heat also contributes to the heat flux at the core mantle boundary and represents an important driver of mantle convection.

Although mineral physics provides us with estimates of the composition and crystalline properties of the inner core, only seismology provides direct measurements of its elastic structure. One of the most striking observations is that the inner core appears to be anisotropic, whereby the velocity of a seismic wave varies depending on its direction of propagation. In the inner core, this anomalous structure is observed in the fact that waves travelling aligned to Earth's rotation axis arrive earlier than waves travelling in the equatorial plane. Later studies showed that these body wave observations are best matched by cylindrical anisotropy (Morelli et al., 1986), which also explains observations of anomalous zonal splitting of inner core sensitive free oscillations (Woodhouse et al., 1986).

As global seismic data coverage increased, seismic investigations began to resolve 3D lateral variations and radial heterogeneity in the inner core. Hemispherical differences were first proposed by Tanaka and Hamaguchi (1997) and later confirmed by many other studies (Niu and Wen 2001; Waszek and Deuss 2011; Lythgoe et al. 2014; Burdick et al. 2019). These hemispherical differences are characterised by a eastern hemisphere with weak anisotropy and fast isotropic velocity, and a western hemisphere

* Corresponding author.
E-mail address: h.brett@uu.nl (H. Brett).

https://doi.org/10.1016/j.epsl.2022.117688

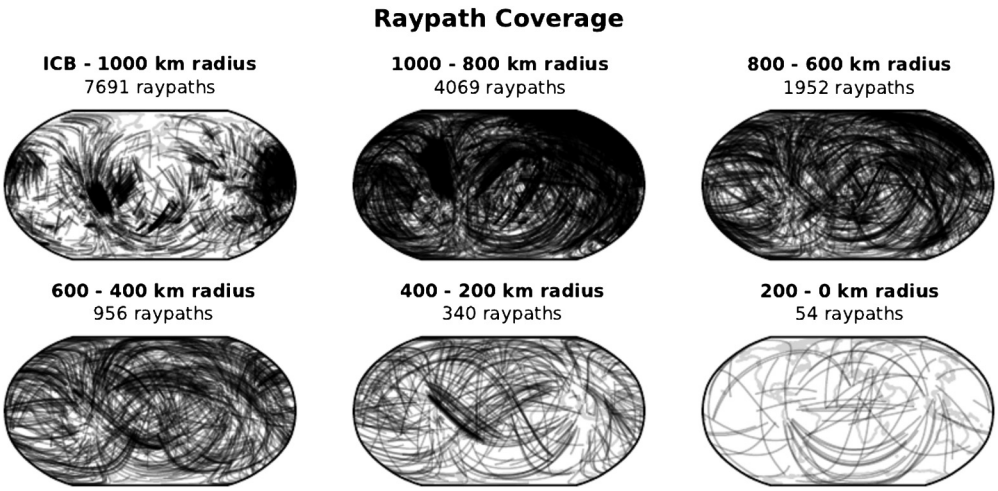

Fig. 1. Raypath coverage of our entire dataset for different layers in the inner core. It shows all raypath segments through each given layer.

with strong anisotropy and low isotropic velocity. The outermost layer of the inner core has been proposed as isotropic, both in the east and west (Wen and Niu, 2002; Waszek and Deuss, 2011). Furthermore, an innermost inner core (IMIC) with a different fast or slow symmetry axes may exist, although the details remain unconfirmed regarding the exact direction of the slow axes, its regional distribution or its origins (Beghein and Trampert, 2003; Ishii and Dziewoński, 2003; Sun and Song, 2008b; Lythgoe et al., 2014; Frost and Romanowicz, 2019). Sun and Song (2008b) produced an impressive early 3D tomographic model of the inner core using differential travel times. Their model recovered many of the main features in the inner core that we still see today, including isotropic quasi hemispheres, an inner most inner core and strong anisotropy in one quasi hemisphere.

One limitation in interpreting seismic body wave observations in terms of distinct regional features (like hemispheres) is that the resultant models strongly depend on the chosen parameterisation. Furthermore, trade-offs exist between different structures depending on the model parameterisation. Not accounting for lateral variations may explain why some studies find a sharp change in anisotropy at an apparent IMIC (Stephenson et al., 2020; Frost and Romanowicz, 2019), while others find a gradual IMIC boundary, if it exists at all (Lythgoe et al., 2014). In addition, hemispheres are often assumed to be defined by meridians and features such as the innermost inner core usually have a constant radius, which may be overly simplifying their shapes.

Another major challenge when imaging the inner core is removing the influence of mantle heterogeneity. A particular subset of raypaths, travelling from the South Sandwich Islands (SSI) to Alaska, have been noted to travel anomalously fast. It has been debated to what extent these travel times reflect inner core structure or mantle structure (Tkalčić 2010; Frost et al. 2020; Brett and Deuss 2020). To address the issue of mantle heterogeneity, we use multiple tomographic mantle models to assess unaccounted for mantle structure, and we develop inner core models which both include and exclude the South Sandwich Islands data.

In this study, we apply a transdimensional Markov Chain Monte Carlo (MCMC) inversion technique (Bodin and Sambridge, 2009) to a large high-quality body wave data set to make a 3D model of inner core velocity and anisotropy. We consider our model to be the next step in inner core tomography, with the main difference that we use a transdimensional Monte Carlo approach and that we can now utilise significantly more data due to the increased coverage of seismic stations and events. The advantage of a transdimensional MCMC methodology over an inversion using a static parameterisation, is that the parameterisation of the model space evolves with the Markov chain and is not predetermined. Thus, the model parameterisation is driven by the data itself, with no prior assumptions on the parameterisation, such as the existence of an IMIC or hemispheres. Previously, Burdick et al. (2019) and Pejić et al. (2019) used a transdimensional MCMC approach to image a single layer of inner core velocity and attenuation respectively. These previous studies were 2D spherical surface inversions and in this paper we go further by conducting the first fully 3D transdimensional MCMC for the inner core, which allows us to resolve jointly for both lateral and radial variations in P-wave anisotropy, which is essential to answering questions on the mechanisms and causes of anisotropy in the inner core.

2. Data and pre-processing

We image the inner core using the phase PKPdf, which travels the mantle, outer core, and inner core as a compressional body wave. PKPdf is used either individually, or in combination with a reference phase (PKPcd, PKPbc, PKPab), which only traverses the mantle and outer core. We employ independent datasets from three previous studies consisting of 1603 PKPbc-PKPdf, 627 PKPab-PKPdf (Brett and Deuss, 2020), and 3102 PKPcd-PKPdf (Waszek and Deuss, 2011) differential travel time measurements, and 2344 absolute PKPdf arrival times (Lythgoe et al., 2014). The arrival times of Brett and Deuss (2020) and Lythgoe et al. (2014) are visual picks, while Waszek and Deuss (2011) used a combination of both visual inspection and cross correlation between the inner core and outer core phases. Combining these datasets provides good coverage of the inner core from its surface to 200 km radius (see Fig. 1). We will need to consider the direction of travel of the PKPdf raypath through the inner core to image anisotropy. For cylindrical anisotropy, we describe the direction of travel by the angle ζ defined as the angle between the PKPdf raypath in the inner core and Earth's rotation axis. We have good raypath coverage for polar raypaths (defined as raypaths with $\zeta < 35°$), which is important for constraining inner core cylindrical anisotropy.

Following the methodology of Creager (1992) we define the fractional differential travel time as:

$$\frac{\delta t}{t} = \frac{(t_{PKPref} - t_{PKPdf})_{data} - (t_{PKPref} - t_{PKPdf})_{Model}}{t} \quad (1)$$

where $(t_{PKPref} - t_{PKPdf})_{data}$ is the observed difference in arrival time between a reference phase and the PKPdf phase, $(t_{PKPref} - t_{PKPdf})_{Model}$ is the theoretical arrival time difference predicted by a model, and t is the inner core travel time of the PKPdf raypath as predicted by a reference model. We use the 1D reference model

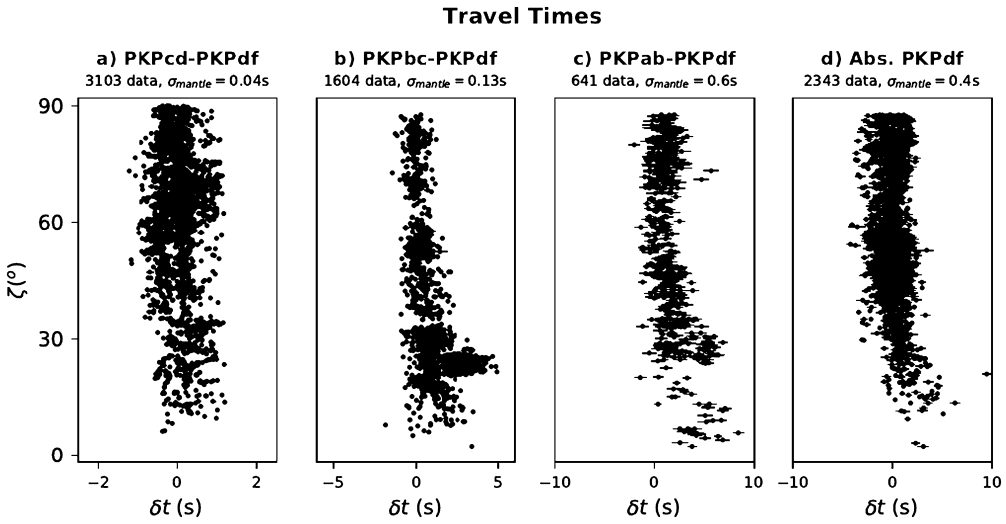

Fig. 2. The variation of mean δt with the angle ζ for a) PKPcd-PKPdf, b) PKPbc-PKPdf, c) PKPab-PKPdf and d) absolute PKPdf differential travel times. The horizontal lines show the standard deviation σ_{mantle} of the δt due to 'mantle noise' from the 6 global P-wave mantle models used. The number of data points and the average of σ_{mantle} is shown in each subtitle. Plots showing the differential travel times for each mantle model, from which the means, are derived are shown in Figs. S2-S3.

AK135 (Kennett et al., 1995). For absolute travel times, we remove the reference phase from the above equation.

Multiple studies have highlighted the significant influence of mantle structure on inner core travel times (Tkalčić 2010; Frost et al. 2020; Brett and Deuss 2020). Mantle corrections will be especially large for absolute travel time measurements, but may also be important for differential travel time data. To correct for the influence of mantle structure and estimate any corresponding uncertainties introduced we calculate differential travel times using six different global P-wave models, integrated across the 1D raypaths from AK135. The global P-wave models used are: UUP07 (Amaru, 2007), MITP08 (Li et al., 2008), GyPSuM, LLNL-G3Dv3 (Simmons et al., 2012), SAW642AN (Panning and Romanowicz, 2006) and SPani (Tesoniero et al., 2015). This results in six synthetic travel times for each PKPcd, PKPbc, PKPab and PKPdf travel time observation in our data set, from which we calculate six different values of δt (Figs. S2-S3). Inspection of Figs. S2-S3 reveals a significant uniform negative shift for the mantle-corrected absolute PKPdf travel times. We expect that this shift is due to 1D mantle structure that differs from the reference model used (AK135); we remove it by subtracting the mean of the mantle-corrected equatorial data from each measurement. Using the six $\frac{\delta t}{t}$ values for each data point for each model, we determine the mean and standard deviation, σ_{mantle}. The standard deviation σ_{mantle} is used as a starting estimate of the noise introduced into the data by the mantle structure which is then extended through hierarchical sampling (see section 4.3).

While the mantle corrections will do a good job of correcting large scale lower mantle structure, strong velocity perturbations locally around events or seismic stations will not be as well resolved by these global tomographic models. However, we assume that such differences will be removed by the differential travel time methodology, because the primary and reference phases are most similar near the source and receiver. As expected, the PKPab-PKPdf and absolute PKPdf data are more affected by mantle structure than the PKPcd-PKPdf and PKPbc-PKPdf data (Fig. 2). Regardless, the mantle corrections in all datasets are an order of magnitude less than the measurements themselves.

3. The forward problem

For a fast direction parallel to Earth's axis of rotation, cylindrical body wave anisotropy in the inner core is defined as follows (Creager, 1992)

$$\frac{\delta t}{t} = \frac{\delta v}{v} = a + b\cos^2(\zeta) + c\cos^4(\zeta) \tag{2}$$

where $\frac{\delta t}{t}$ is equivalent to the velocity anomaly $\frac{\delta v}{v}$ (assuming low attenuation in the inner core). The difference in the velocity of equatorial raypaths relative to the reference model (AK135), δV_{eq}, is given by a in Equation (2). The amount of anisotropy, δV_{ani}, is defined as the velocity difference between polar and equatorial raypaths, given by $b + c$. This measure of anisotropy is strictly for cylindrical anisotropy, and assumes that the slow and fast directions are perpendicular. The b and c parameters of Equation (2) are related to components of the elastic tensor, C_{ij}, which describes the anisotropy of a medium by $b = (C_{33} - C_{11})/2C_{11}$ and $c = (4C_{44} + 2C_{13} - C_{11} - C_{33})/8C_{11}$ (Creager, 1992). From the model parameters a, b and c we calculate the isotropic velocity, or Voigt average velocity (Lythgoe et al., 2014) commonly interpreted by mineral physicists;

$$\delta V_{iso} = a + \frac{b}{3} + \frac{c}{5} \tag{3}$$

Equation (2) reveals that the slowest velocity direction is not restricted to an angle of $\zeta = 90°$, but depends on combinations of b and c, thus can be any angle between $0 - 90°$. The slowest angle is obtained by differentiating Equation (2) and calculating its maximum value, following Lythgoe et al. (2014), which results in the following:

$$\zeta_{slow} = \cos^{-1}\sqrt{\frac{-b}{2c}} \tag{4}$$

Some variations in ζ_{slow} are statistically insignificant: it is possible to have a large range of values of ζ_{slow} but with minimal absolute velocity differences between ζ_{slow} and $\zeta = 90°$. To only keep statistically significant values of ζ_{slow}, we use a tolerance condition, such that the difference between ζ_{slow} velocity and that at $\zeta = 90°$ must be greater than 0.5% of the reference velocity. We will present our model showing variations in δV_{eq}, δV_{iso}, δV_{ani}, and ζ_{slow}. It is important to note that throughout this paper we define anisotropy to be the difference between the polar and the equatorial velocity (as is conventional for body wave studies of the inner core). However, in some regions of our model the difference between the polar and equatorial velocity is small ($\delta V_{ani} \sim 1.0\%$) while the difference between the ζ_{slow} direction and the $\zeta = 0°$

is stronger (∼2.0%). These regions should still be thought of as anisotropic even though the value of δV_{ani} is small.

For a single raypath with ζ and set of coefficients (a, b, c) we predict the normalised differential travel time using Equation (1). However, this treats the inner core as a homogeneous volume, whereas we are interested in 3D variations. For an inner core with multiple sub-volumes, we split the ray into different portions for each model sub-volume travelled, resulting in the following linear forward problem:

$$\mathbf{Gm} = \mathbf{d}_{syn} \tag{5}$$

$$\mathbf{G} = \begin{pmatrix} A_{1,1}t_1 & A_{1,1}t_1\cos^2(\zeta) & A_{1,1}t_1\cos^4(\zeta) & A_{1,2}t_1\cdots \\ A_{2,1}t_2 & A_{2,1}t_2\cos^2(\zeta) & A_{2,1}t_2\cos^4(\zeta) & A_{2,2}t_2\cdots \\ A_{3,1}t_3 & A_{3,1}t_3\cos^2(\zeta) & A_{3,1}t_3\cos^4(\zeta) & A_{3,2}t_3\cdots \\ \vdots & \vdots & \ddots & \end{pmatrix} \tag{6}$$

$$\mathbf{m} = \begin{pmatrix} a_1 \\ b_1 \\ c_1 \\ a_2 \\ \vdots \end{pmatrix} \tag{7}$$

$$\mathbf{d} = \begin{pmatrix} \delta t_1 \\ \delta t_2 \\ \delta t_3 \\ \vdots \end{pmatrix} \tag{8}$$

where **G** is the sensitivity kernel matrix which has the same number of rows as the number of travel times in our dataset, and the same number of columns as the length of vector **m**. $A_{i,j}$ within **G** is a value between 0 and 1 describing the fraction of raypath i which travels through volume j and $\sum_{j=1}^{N} A_{i,j} = 1$ for a total of N volumes. The model vector, **m**, contains the parameters a_j, b_j, c_j for each volume j. **d** is the data vector containing the differential travel time δt_i of each raypath i. Note that the inner core travel time t_i has been moved from the left hand side in Equation (2) to the right hand side, and is now part of matrix **G**. In a static MCMC, the parameterisation of the sensitivity kernel matrix **G** remains constant, forming a fixed forward problem. In the transdimensional MCMC, the sensitivity kernel matrix **G** changes at each step of every new model parameterisation.

Calculating the $A_{i,j}$ terms is a function of the raypath discretisation and the basis functions used. For this study, we use fixed raypaths as modelled by AK135 using the Taup Toolkit (Crotwell et al., 1999) and assume the inner core is spherical (note that we do correct our data for ellipticity using the methodology of Dziewonski and Gilbert, 1976). We do not adjust the raypaths in our model using 3D raytracing. The transdimensional inversion is already a computationally expensive non-linear inversion and tests incorporating 3D raytracing through an anisotropic model significantly increased the time taken to approximate the posterior making it unfeasible. Therefore, we decided that for this study it was sufficient to use fixed raypaths and assess the uncertainties in the travel times through hierarchical sampling.

The basis functions are 3D Voronoi cells, which provide a fast method of tessellating a domain with non-overlapping volumes.

4. The inverse problem

4.1. Bayes' theorem

We solve the inverse problem using a Bayesian approach, where we do not consider one single solution but instead regard the solution to be a collection of models (an 'ensemble') from which uncertainties can be determined. In practice, the Bayesian approach combines prior information on a model space with data to produce a posterior probability distribution. Following Bodin and Sambridge (2009), the posterior probability $p(\mathbf{m}|\mathbf{d}_{obs})$ is given by

$$p(\mathbf{m}|\mathbf{d}_{obs}) \propto p(\mathbf{d}_{obs}|\mathbf{m})p(\mathbf{m}) \tag{9}$$

where the *likelihood* function $p(\mathbf{d}_{obs}|\mathbf{m})$ is the probability of observing a set of data given a set of model parameters. The *prior* function $p(\mathbf{m})$ describes our knowledge of the model space before considering the data. The posterior $p(\mathbf{m}|\mathbf{d}_{obs})$ represents how the data and our prior knowledge combine, providing us with the probability that a given set of model parameters are true.

4.2. Markov chain Monte Carlo

We then use Markov Chain Monte Carlo (MCMC) to sample the posterior probability distribution of our data-model system (Cowles and Carlin, 1996). For a given prior probability and data, we evaluate the forward problem over many proposed models, with each proposed model related to the previous model with a small random perturbation. After randomly perturbing an initial model, we use the Metropolis-Hastings algorithm (Hastings 1970) to probabilistically accept or reject perturbations. The Metropolis-Hastings criteria ensure that accepted models are representative of the posterior probability distribution.

4.3. Likelihood and hierarchical noise

The likelihood function, $p(\mathbf{d}_{obs}|\mathbf{m})$, describes how well a set of model parameters reproduces the data:

$$p(\mathbf{d}_{obs}|\mathbf{m}) \propto \exp\frac{-\phi(\mathbf{m})}{2} \tag{10}$$

where ϕ is the least squares misfit of a model normalised by data noise. We use an L2 norm which is frequently used in seismic tomography:

$$\phi(\mathbf{m}) = \left|\left|\frac{\mathbf{d}_{syn} - \mathbf{d}_{obs}}{\lambda_d}\right|\right|^2 \tag{11}$$

where d_{syn} is the synthetic data predicted by the model **m** (calculated using Equation (5)), λ_d is the hierarchical parameter and is the estimated data noise. λ_d has a profound influence on the MCMC because the algorithm will only fit the data to within this noise limit. Thus, λ_d is analogous to the damping parameter in a damped least squares inversion. However unlike the damping parameter, it is possible to assess the value of λ_d from the data itself using hierarchical methods. We separate λ_d into $\lambda_{DataType}$ for each data type, since the four data types (PKPcd, PKPbc, PKPab differential travel times and absolute PKPdf travel times) have different levels of noise. For each individual δt data point we use the mantle noise, σ_{mantle}, estimated from the six global tomographic models (see section 2) as a minimum level of noise. From this, each measurement then has its own $\lambda_d = \sqrt{\lambda^2_{DataType} + \sigma^2_{mantle}}$. The misfit then becomes:

$$\phi(\mathbf{m}) = \sqrt{\sum_{n=1}^{N_{Data}} \left(\frac{(\mathbf{d}_{syn} - \mathbf{d}_{obs})_n}{\sqrt{\lambda^2_{DataType} + \sigma^2_{mantle,n}}}\right)^2} \tag{12}$$

The hierarchical parameter $\lambda_{DataType}$ is not a term that we choose, but is sampled as an additional perturbation step in the MCMC, which is also accepted following the Metropolis-Hastings algorithm. In this way, $\lambda_{DataType}$ estimates the noise by examining contradictions within the data itself, and combining this with

the prior estimate of the data noise from the tomographic models. For example, if two or more observations that sample the same region of the model are contradictory then they will be fit poorly and drive the hierarchical parameter to higher values indicating a greater level of uncertainty in the data. This approach handles data uncertainties thoroughly, using the estimates of σ_{mantle} from the tomographic models to provide a minimum misfit on individual data points, then using the $\lambda_{DataType}$ terms to maintain an overview of the noise of each subset of data. Substituting Equation (12) into Equation (10) provides us with the first term on the right hand side of Equation (9).

4.4. Prior

The prior, $p(\mathbf{m})$ (the second term on the right hand side of Equation (9)), is a probability distribution function representing any knowledge on the physical system before data is considered. We use Gaussian probability distributions for model parameters, a, b and c with a mean of 0 and a standard deviation, σ, of 0.1 (or 10% velocity perturbations relative to AK135). That is, for the ith a parameter we have in our model we have:

$$p(a_i) = \frac{1}{\sigma\sqrt{2\pi}} \exp(-\frac{a_i^2}{2\sigma}) \tag{13}$$

with the same equation for b and c, giving a prior of the form:

$$p(\mathbf{m}) = \prod_i p(a_i)p(b_i)p(c_i). \tag{14}$$

This prior reflects current knowledge on inner core structure while not restricting the size of the model space prohibitively. For example, it has the capacity to incorporate anisotropy $(b + c)$ of 10% in our model. We consider Gaussian priors to be more appropriate than uniform priors as uniform priors can overly restrict the size of the model space.

4.5. Transdimensional model proposals

In a traditional MCMC inversion the parameterisation of the model space is static (i.e. the number and locations of the Voronoi cells remains the same across all iterations) and defined prior to the inversion. Thus, only the model parameters a, b and c within each Voronoi cell would be perturbed. However, in our transdimensional MCMC, the data defines how the model is parameterised through perturbing the number and locations of the Voronoi cells. Thus, the transdimensional method samples models with different complexity (i.e. number of model parameters and volumes) resulting in an ensemble of varying dimensioned models that plausibly explain the observations. This is implemented as a 'reductionist' methodology, i.e. if the dataset can be fit equally well with 10 volumes instead of 11, then the final ensemble will include more models with 10 volumes than 11.

The velocity perturbations to the model parameters a, b and c are described in Appendix B.1. The additional perturbations to the parameterisation of the model space require three more perturbation types: *move* (moving cells), *birth* (generating new cells), and *death* (removing cells) and are described in detail in Appendix B.2-B.4.

5. Ensemble analysis

We applied the transdimensional MCMC algorithm (section 4.5) to our data (section 2) and ran 20 chains for 4,000,000 iterations with an acceptance rate (the percentage of accepted perturbations) of 30.5%. Fig. 3a shows how the misfit changes as a function of iteration in the inversion for all 20 chains. The misfit drops rapidly

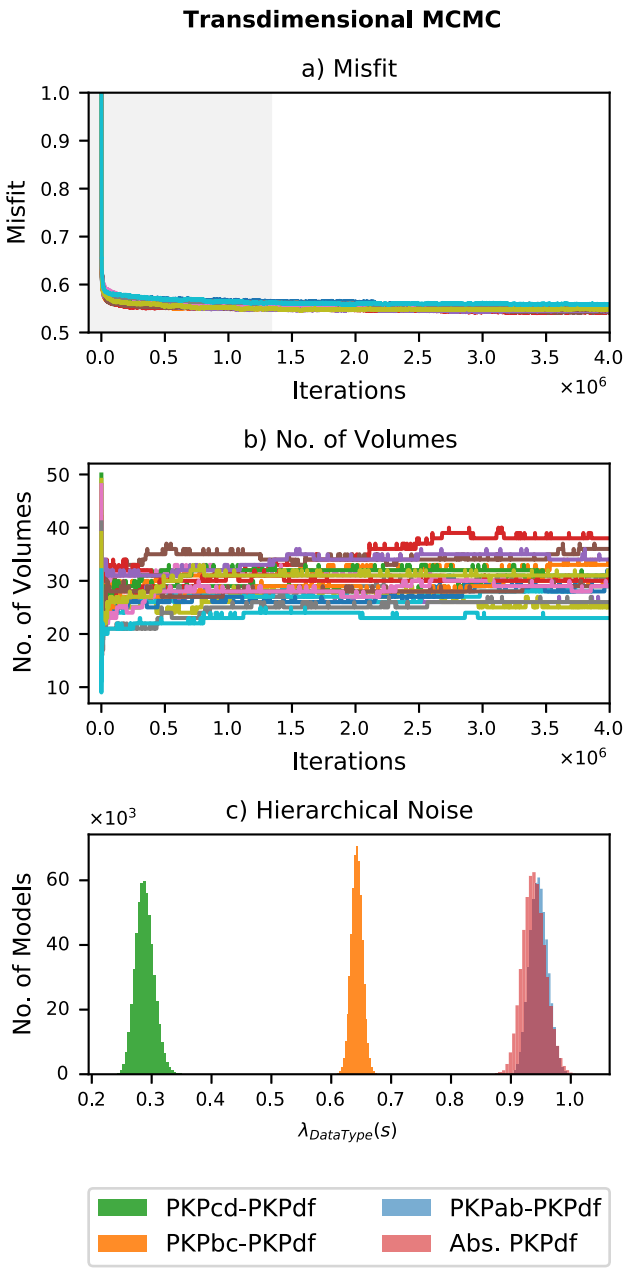

Fig. 3. a) Variation of misfit with iteration in all 20 chains for our transdimensional model. b) Variation of no. of volumes with iteration in all 20 chains for our transdimensional model. The greyed out area in a) & b) is the 'burn in'. c) The total hierarchical parameter of each of our data types, i.e. $\lambda^{total}_{DataType} = \sqrt{\lambda^2_{DataType} + mean(\sigma^{DataType}_{mantle})^2}$ calculated from the ensemble from our transdimensional model. (For interpretation of the colours in the figure(s), the reader is referred to the web version of this article.)

in the first 200,000 iterations before reaching a misfit minimum; the transdimensional algorithm then samples models around this minimum value.

Once the inversion has completed the desired number of iterations, the models are collected into an ensemble from which statistics are calculated. We remove the influence of the starting model by excluding the first third of all iterations in the ensemble of models; the so-called 'burn in'. It is also common practice to 'thin' the chain by only retaining every 100th model, which ensures that each model in an ensemble is independent. Following 'burn in' and 'thinning' leaves a final ensemble of 533,380 models.

For further discussion regarding appropriate values for the 'burn in' and 'thinning' we refer the reader to Cowles and Carlin (1996).

For an MCMC investigation, it is important to ensure that the model sampling has converged, whereby the model space has been sufficiently explored and the models are no longer evolving substantially. To assess convergence, we examine the number of volumes in each chain as a function of iteration (Fig. 3b). The number of volumes across all chains drops rapidly within the first 10,000 iterations, as the starting model is refined and Voronoi cells which do not reduce misfit are removed. After this initial reduction of volumes, the MCMC algorithm better assesses the noise level within the data, and the number of volumes across all chains starts to increase before flattening out after 1,000,000 iterations. For the next 3,000,000 iterations, the mean number of volumes across all chains does not change substantially, implying convergence. After convergence, the average model misfit has reduced from 1.0 to 0.55, and the models have between 23 and 38 volumes.

We also investigate the average hierarchical noise parameters for each data type (section 4.3) from the 533,380 models in our final ensemble (Fig. 3c). As expected, the PKPcd-PKPdf data has the lowest noise level with 0.29 s on average of uncertainty in each measurement, followed by PKPbc-PKPdf data with a noise level of 0.63 s. Finally, the PKPab-PKPdf data and absolute PKPdf data show the largest levels of noise with similar values of approximately 0.95 s. Thus, the hierarchical sampling found the PKPcd-PKPdf data to have the lowest noise level, and will fit those observations more closely than the PKPab-PKPdf and absolute PKPdf data. From this analysis we expect that the top of the inner core is the best resolved region of our model due to the low noise level in the PKPcd-PKPdf data and the fact that we have more data sensitive to the top of the inner core than the centre of the inner core.

6. Results

Our final model was generated by calculating the mean and standard deviations of four different model parameters from the a, b and c values of the 533,380 models in our ensemble: the equatorial velocity (δV_{eq}), the isotropic or Voigt average velocity (δV_{iso}), the anisotropic velocity difference (δV_{ani}), and the angle of slowest direction (ζ_{slow}) (see section 3). Models in our ensemble will contain different numbers of Voronoi cells at different locations and these individual models will contain sharp boundaries. However when we average across all 533,380 models the boundaries will not be in exactly the same place in every model, meaning that the average model can contain smoothly varying and irregular shaped boundaries.

We will explore our results in terms of large-scale general observations that have been seen before, including the isotropic hemispheres (section 6.1), the anisotropic zone (section 6.2) and the inner most inner core (section 6.3), but mainly focus on the finer-scale details which have become obvious because of our transdimensional approach.

6.1. Isotropic hemispheres

Our model confirms the previously found hemispherical pattern with seismic P-waves travelling anomalously fast in the 'eastern hemisphere' of the inner core and anomalously slow in the 'western hemisphere'. This is evident in maps of equatorial velocity throughout the inner core (Fig. 4a-c), and at the top of the inner core in isotropic velocity (Fig. 4g). The hemispherical pattern is also clearly visible in cross sections through the equatorial plane (Fig. 5a,c) and meridional cross sections through the North and South pole (Fig. 6a,c). This is in agreement with numerous previous studies (Tanaka and Hamaguchi 1997; Niu and Wen 2001; Waszek and Deuss 2011; Lythgoe et al. 2014; Burdick et al. 2019; Brett and Deuss 2020). We avoid describing the hemisphere boundaries using single meridians because the hemisphere boundaries are not straight lines through the poles; this is most visible in the equatorial velocity at the ICB around southern Africa and Hawaii (Fig. 4a.)

It is interesting to note that the hemispherical pattern in the equatorial velocity (Fig. 5a and 6a) persists and the magnitude of the equatorial velocity increases with depth in the eastern hemisphere. The advantage of our use of the transdimensional approach, is that we are not limited to simple hemispherical shapes anymore and so are now able to identify regional heterogeneity within the hemispheres. Further complexity is particularly visible in the meridional cross section (Fig. 6a), which reveals that the boundary separating the fast and slow equatorial velocities appears sharp and undulating. Some faster equatorial velocities associated with the eastern hemisphere encroach on the slower velocities of the western hemisphere. These new observations would be challenging to identify robustly without using a transdimensional methodology, as it would be difficult to know the extent to which the final model was influenced by the initial fixed parameterisation.

Comparing our model of the equatorial velocity to that of Burdick et al. (2019) we see good overall agreement in the location of the hemisphere boundaries, but with some extra complexity, this is due to the fact that we also solve for the 3D velocity structure and have more data both of which will influence the location of the boundaries at the ICB.

The hemispherical pattern in the isotropic velocity is present until about 60-170 km depth below the ICB (Fig. 4g, 5c and 6c), with boundaries between slow 'west' and fast 'east' located approximately at 170°W and 30°E in broad agreement with previous studies (Tanaka and Hamaguchi 1997; Waszek and Deuss 2011; Burdick et al. 2019). The reason that the isotropic velocity difference does not persist deeper in the inner core, is because the isotropic velocity is a Voigt average of the velocities in all directions. Although the hemispherical variations persist in the equatorial velocity with depth, the contribution of anisotropy (i.e. higher polar velocities) causes the isotropic velocity to lose its hemispherical pattern deeper than 60-170 km below the ICB (Fig. 7a).

6.2. Anisotropic zone

In agreement with previous studies (i.e. Tanaka and Hamaguchi 1997; Niu and Wen 2001; Lythgoe et al. 2014; Brett and Deuss 2020), our model also contains a strong anisotropic zone in the west where inner core seismic P-waves travelling in the north-south or polar direction travel faster than waves that travel in the east-west or equatorial direction. The lateral extent of the western anisotropic zone is clearly visible in maps of the anisotropic velocity difference (Fig. 4n-o) at 400 and 800 km radius and also in cross-sections through our model (Fig. 5e and 6e). The inner core displays very little anisotropy near the ICB (Fig. 4m), with the exception of a strong patch with high uncertainty around South America, similar in location to a high uncertainty region found in Pejić et al. (2019).

A 1D profile through our model (Fig. 7a) furthermore shows that indeed anisotropy is weak at the top of the inner core (0 to 1%) and confirms strong anisotropy to be located within the western hemisphere approximately between 50 and 1100 km radius, and only weak anisotropy ($< 0.5\%$) in the eastern hemisphere. The anisotropic strength increases rapidly with depth, reaching a maximum of 7.2% in the western hemisphere. The radius of the transition to strong anisotropy in this region occurs between 1170 km and 1050 km (Fig. 7a). It is difficult to define more precisely this radius due to a lack of raypaths with turning points between

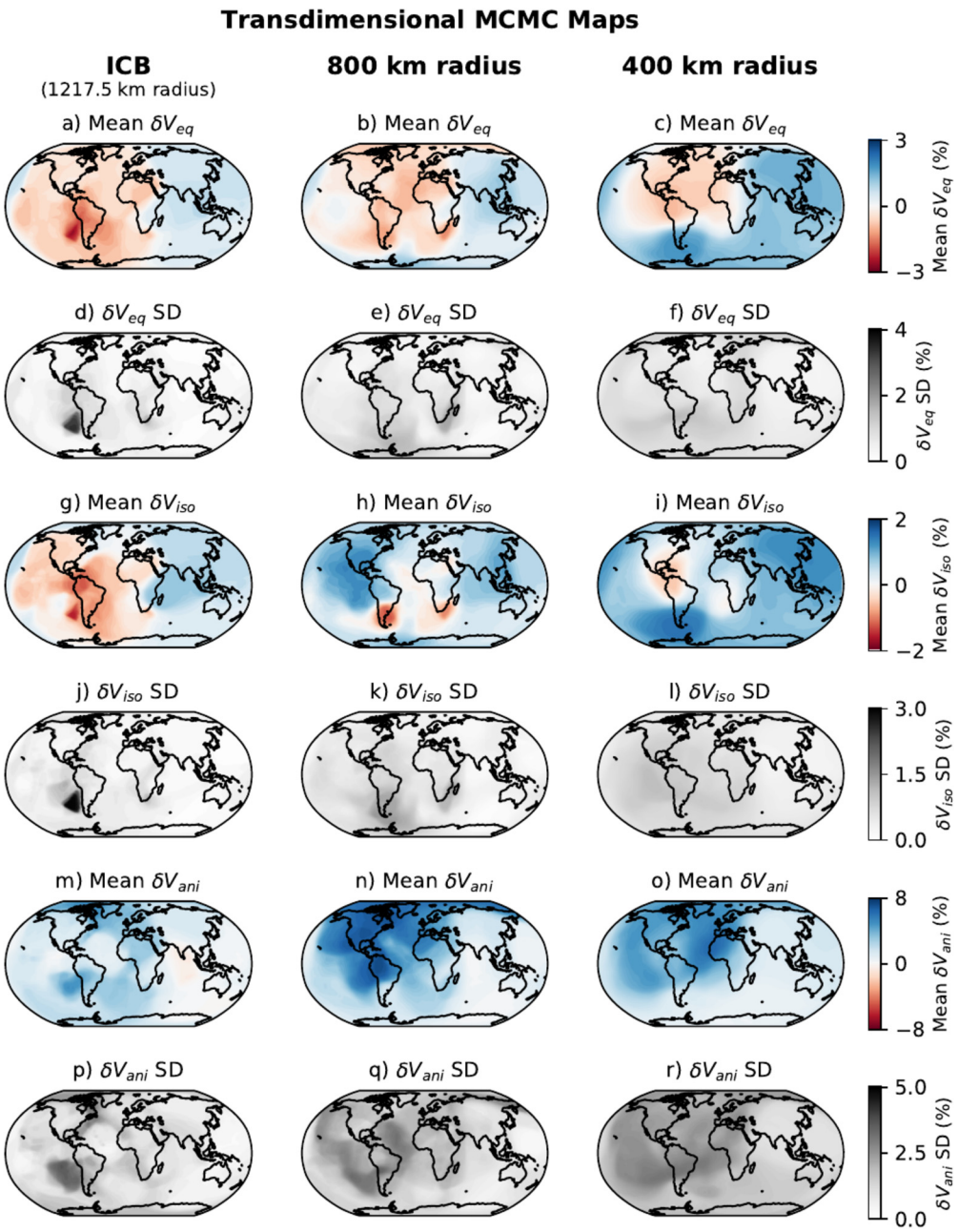

Fig. 4. Maps of the mean and standard deviation (SD) of δV_{eq}, δV_{ani} and δV_{iso} at the ICB (1217.5 km radius), 800 km radius and 400 km radius throughout our model. The same plot showing a transdimensional inversion using the same model setup but excluding data originating from the South Sandwich Islands is shown on Fig. S16.

1110 km and 1060 km (Blom et al., 2015), resulting in a partial null space. This lack of data is reflected in the standard deviation (Fig. 5f), which shows a broad region of high uncertainty at the top of the anisotropic zone.

Tanaka and Hamaguchi (1997) described the anisotropic zone as being a 'quasi-hemisphere', i.e. it does not precisely span 180° of longitude. Indeed, we also observe that the anisotropic zone does not span 180° but runs between 170°W and 30°E (Fig. 5e), spanning a width of 200° in broad agreement with previous models (Sun and Song 2008a; Irving and Deuss 2011; Lythgoe et al. 2014).

Most importantly, because of our transdimensional approach we do not prescribe simple hemispherical shapes; this enabled us to find that the anisotropic zone does not continue all the way to the south pole. Instead, we observe for the first time that the western anisotropic zone is largely confined to the northern hemisphere (Fig. 6e). The anisotropy at the South pole of the inner core at 800 km radius is 2% with an uncertainty of 1.5%, while the anisotropy around North America is 8% with an uncertainty of 2% (Fig. 6e) meaning that within the bounds of uncertainty in our model the South pole has significantly lower anisotropy than the region around North America. This regional feature would have been difficult to map using traditional seismic tomography employing fixed parameterisations, and has important implications for models of inner core growth (section 7). Given that this region of strong anisotropy does not span half the inner core in either longitude or latitude, we use the descriptor of an 'anisotropic zone' (instead of hemisphere).

We conducted a resolution test, to ensure the concentration of anisotropy in the northern part of the western hemisphere was not an artefact of imperfect data coverage. To do this, we ran an inversion using synthetic data for a known synthetic model, con-

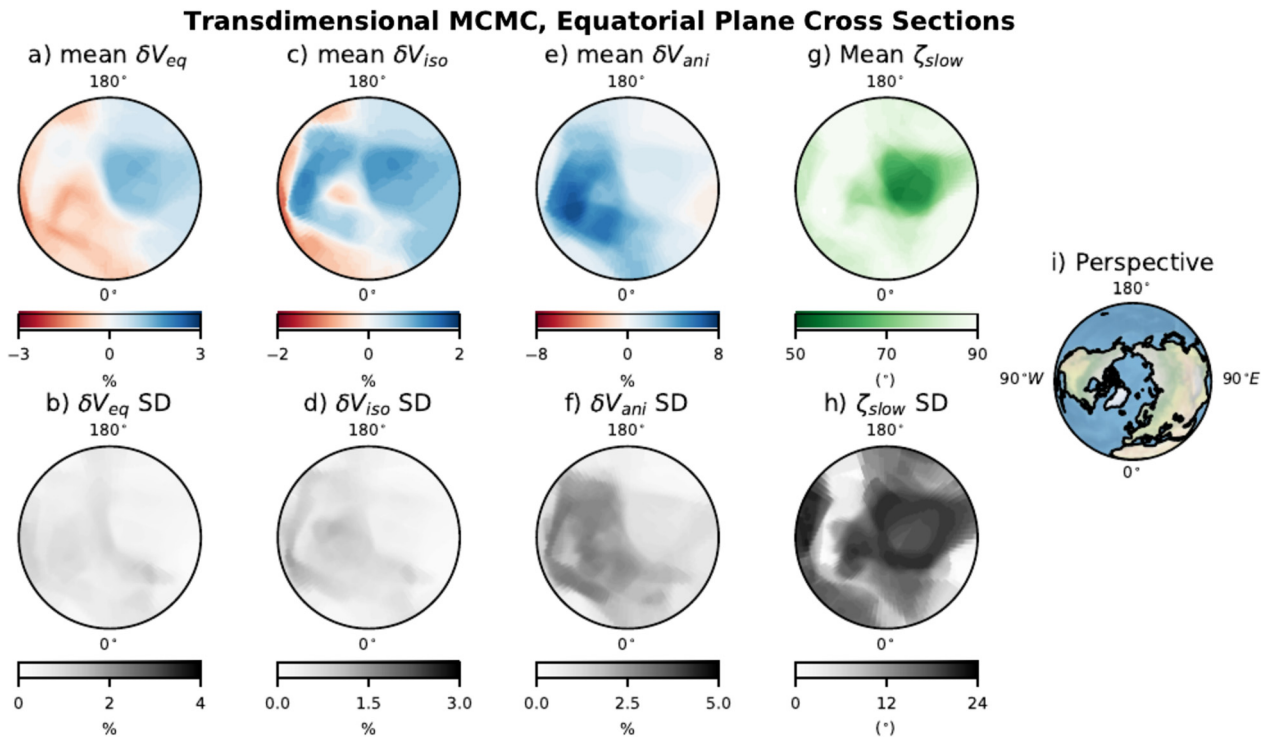

Fig. 5. Cross sections showing the average and standard deviation (SD) of the δV_{eq}, δV_{ani}, δV_{iso} and ζ_{slow} variations throughout our model. The cross section is a horizontal slice through the equator with constant latitude. The view of the reader is shown in the perspective panel. The same plot showing a transdimensional inversion using the same model setup but excluding data originating from the South Sandwich Islands is shown on Fig. S19.

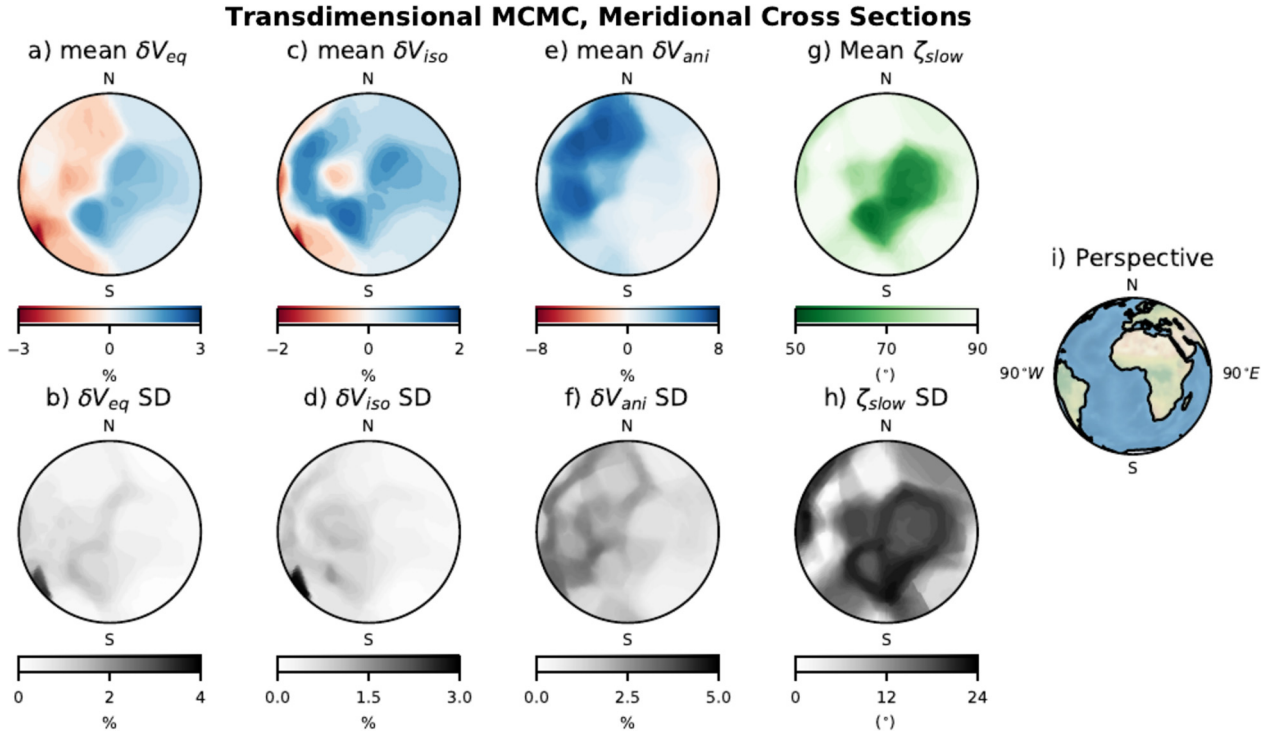

Fig. 6. Cross sections showing the average and standard deviation (SD) of the δV_{eq}, δV_{ani}, δV_{iso} and ζ_{slow} variations throughout our model. The cross section is a vertical slice spanning all latitudes and going from 90°W to 90°E. The view of the reader is shown in the perspective panel. The same plot showing a transdimensional inversion using the same parameters but excluding data originating from the South Sandwich Islands is shown on Fig. S18.

taining simple hemispheres (with 8% anisotropy and 0% equatorial velocity in the west and 0% anisotropy and 2% equatorial velocity in the east) spanning all latitudes and a spherical IMIC (with 0.5% anisotropy and 1% equatorial velocity) located at the centre of the model (Figs. S9-S11). From this model we generated synthetic data using our real raypaths and added realistic Gaussian noise. The same transdimensional inversion was then conducted on the synthetic data as for the real data. We reproduced all major features from the synthetic model reliably (Figs. S12-S15), including an anisotropic hemisphere across all latitudes. This confirms that

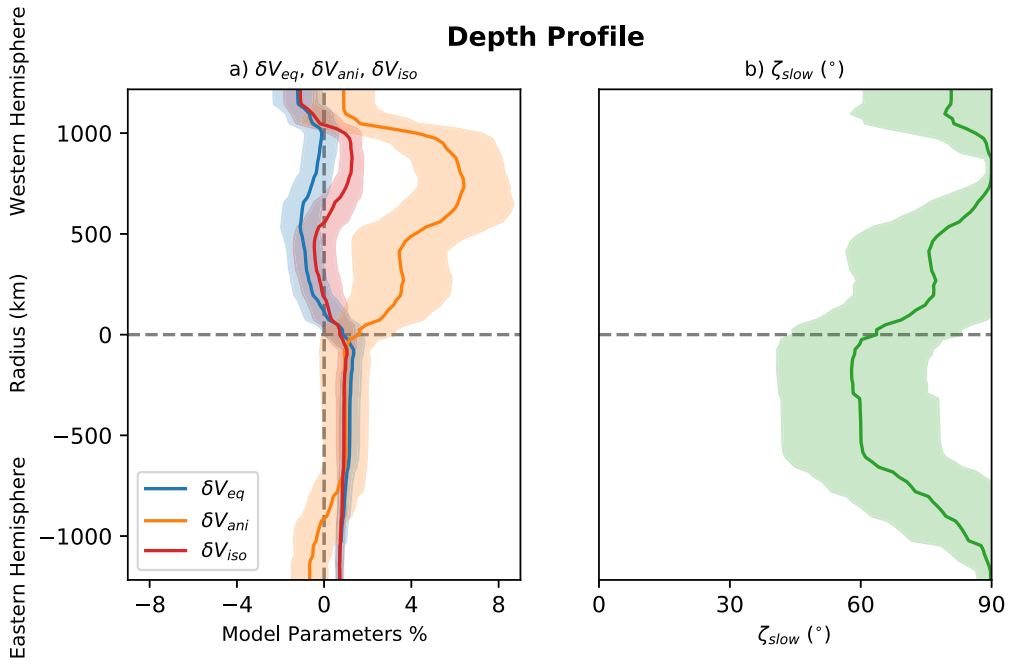

Fig. 7. A profile through the inner core going from 90°W,0°N at the top to 90°E,0°N at the bottom. a) Shows the mean and standard deviation (SD) of δV_{eq}, δV_{ani}, δV_{iso} while the profile on b) shows the variations in ζ_{slow} direction throughout our model.

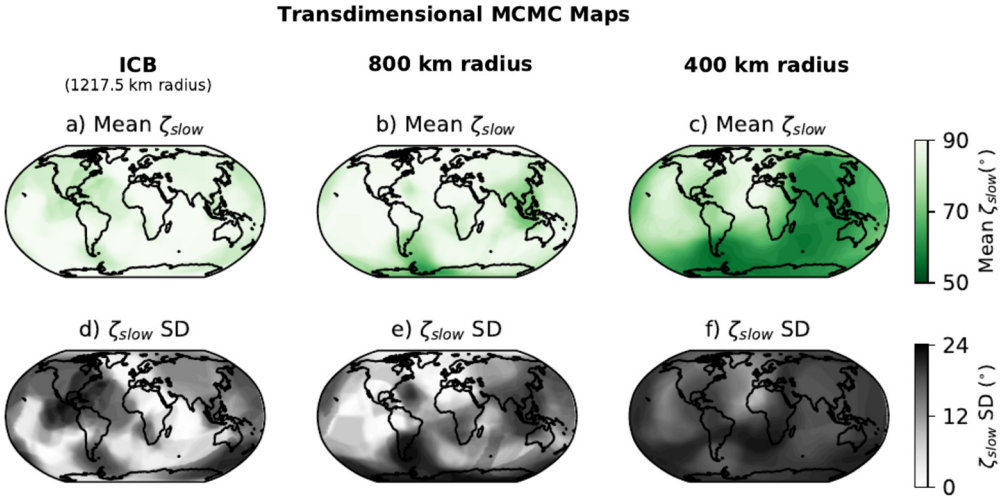

Fig. 8. Maps of the mean and standard deviation (SD) of ζ_{slow} at the ICB, 800 km radius and 400 km radius throughout our model. The same plot showing a transdimensional inversion using the same model setup but excluding data originating from the South Sandwich Islands is shown on Fig. S17.

if the anisotropic region in the west of the inner core spanned all latitudes our data would be able to recover this feature.

We also ran a separate inversion excluding the particular subset of raypaths travelling from the South Sandwich Islands to Alaska (Figs. S16-S19). These raypaths appear to travel anomalously fast, and it has been debated to what extent these travel times reflect regional-scale inner core structure versus mantle contamination (Tkalčić 2010; Frost et al. 2020; Brett and Deuss 2020). Our model excluding SSI data shows the same main features, in particular that the western anisotropic zone is still located primarily in the northern hemisphere. Thus, we conclude that the effect of the SSI data on our inversion is minimal and that the western anisotropic zone is indeed confined to the northern hemisphere.

6.3. Offset IMIC

The inner most inner core (IMIC) has been defined in previous studies as a anisotropic region where the slowest direction (i.e. ζ_{slow} of equation (4)) is at an angle smaller than 90 degrees from the fastest direction. ζ_{slow} is harder to constrain than δV_{eq} and δV_{ani} since variations in ζ_{slow} produce a more subtle effect on P-wave travel times. Despite this, we detect a clear region in which ζ_{slow} is $55° \pm 16°$; this is most notable in the cross-sections through our model (Figs. 5g and 6g). Within this region, δV_{ani} (the difference between purely polar paths with $\zeta = 0°$ and equatorial paths with $\zeta = 90°$ is small ($\sim 1\%$). What matters here instead, is that the difference in velocity between polar paths with $\zeta = 0°$ and paths with ζ_{slow} is as large as 2% and therefore, despite having a small value of δV_{ani} this region should still be considered anisotropic.

Interestingly, it appears not to be a spherical feature at the centre of the inner core. In fact, the centre of the IMIC in our model is offset from the centre of the inner core by approximately 400 km, and our IMIC is contained within the eastern hemisphere (Fig. 7b and Fig. 8c). Our 'non-spherical' or offset IMIC appears to recon-

cile previous differing IMIC models (Ishii and Dziewoński, 2003; Beghein and Trampert, 2003; Sun and Song, 2008b; Lythgoe et al., 2014; Frost and Romanowicz, 2019). The model of Sun and Song (2008b) was an early 3D inner core model which observed an IMIC, in their model the parameterisation of the IMIC was fixed, with the IMIC in the central 600 km of the inner core. However, Sun and Song (2008b) also ran a model without a fixed IMIC. They concluded that their model with and without a fixed IMIC was approximately the same and that the IMIC was spherical. However, looking at their model again it seems possible that they were already seeing evidence of an offset IMIC but did not have the data at the time to be certain. Lythgoe et al. (2014) went further and proposed that the IMIC is in fact part of a larger hemispherical pattern which is in effect what we still see in our model today with more data and a more advanced technique.

We ensured that this offset is not an artefact of data coverage by running two synthetic tests. In one test we included a central spherical IMIC in our synthetic model (Figs. S9-S11) and produced synthetic data. After running a transdimensional inversion with this synthetic data we were able to resolve this regional feature (Figs. S12-S15), showing that if the IMIC was spherical our data would be able to resolve this. In the second synthetic test we used an offset IMIC which was only present in the eastern hemisphere (Figs. S20-S21) and we were also able to fully recover this synthetic model after running a transdimensional inversion (Figs. S22-S23).

6.4. Summary

Summarising the findings from our model, we identify three robust and particularly interesting features in our model:

1. Strong anisotropy is isolated to a zone within the western hemisphere. The anisotropy is strongest north of the equator and weakens to virtually no anisotropy near the south pole. The top of the inner core near the ICB displays very little anisotropy, however, anisotropy increases sharply below 200 km depth in the west.
2. We interpret a region with $\zeta_{slow} = 55° \pm 16°$, located primarily in the eastern hemisphere at a radius less than 700 km as the IMIC, with the centre of the IMIC offset from the centre of the inner core by 400 km.
3. Equatorial and isotropic velocity anomalies are separated into two hemispheres, with a slow western hemisphere and a fast eastern hemisphere. The isotropic velocity difference between the hemispheres is present in the top 60-170 km of the inner core, and disappears at greater depth. The hemispherical pattern in equatorial velocity, on the other hand, persists to the centre of the inner core with the equatorial velocity increasing with depth in the eastern hemisphere.

7. Geodynamic implications

Relating our seismic observations to geodynamical processes in the inner core is challenging due to the multiple mechanisms proposed to explain the formation of anisotropy and the generation of hemispheres. It is now widely accepted that anisotropy is caused by the alignment of iron crystals, which occurs either during solidification or afterwards through texturing. However, the phase of iron which is stable at inner core conditions remains debated. At inner core temperatures and pressures iron takes the form of hcp (hexagonal close packed), bcc (body centred cubic), or fcc (face centred cubic) crystals. Each phase displays varying intrinsic anisotropy, although the magnitude of anisotropy observed seismically also depends on the degree of crystal alignment. In order to test if our seismic observations would be able to constrain the phase of iron, we calculated the anisotropy of a single crystal of each phase of iron at inner conditions using values obtained by ab initio simulations from Vočadlo (2007) and Martorell et al. (2015) and calculated the corresponding seismic travel times (see Fig. S7). The precise magnitude of anisotropy of these phases of iron at inner core temperatures and pressures remains an open question and while hcp iron seems the most likely candidate to account for observed inner core anisotropy, fcc iron is yet to be ruled out. Details on calculating the velocity characteristics of single crystals of iron can be found in Appendix B.5.

To facilitate the comparison between the single crystal anisotropy from the mineral physics and the anisotropy variations in our models, we used the mean a, b, and c parameters from our models for three different locations and plot the corresponding predicted fractional travel times (Fig. 9a). We select locations from the western anisotropic zone (90°W, 0°N, 800 km radius), the IMIC (90°E, 0°N, 100 km radius), and the eastern hemisphere (90°E, 0°N, ICB). The western zone clearly exhibits strong cylindrical anisotropy, whereby polar raypaths are 5.9% faster than equatorial. There is negligible anisotropy in the eastern hemisphere ($< 0.5\%$), and rays which travel in a polar direction are slower than equatorial rays. In the IMIC, the equatorial and polar velocities are similar; the slowest direction is oriented at $\zeta = 55°$, with a velocity decrease of almost 2% relative to the polar velocity.

The anisotropy in the western zone (Fig. 9a) appears most similar to the anisotropy predicted for a single hcp crystal with symmetry axis aligned N-S (Fig. 9b), while anisotropy in the IMIC is more complex. Polar raypaths passing through the IMIC are only slightly faster than the equatorial raypaths; the largest travel time difference is instead between the slowest direction (at $\zeta = 55°$) and the equatorial and polar directions. This anomalous anisotropy could be caused by the dominance of the bcc or fcc iron phases with a tilted fast symmetry axis. For example, If we align the anisotropy symmetry axis with the fastest direction through a bcc or fcc crystal (which is at $\zeta = 54°$, see Fig. S7) then we get the predicted travel times shown in Fig. 9c. The travel times for fcc and bcc (Fig. 9c) bear a resemblance to the anisotropy we observe in the IMIC (Fig. 9a). It is important to note, that this analysis is an approximation as we are assuming that the anisotropy of a large volume made of many crystals can be described by a single crystal with 100% alignment relative to Earth's axis of rotation. We are, however, making this comparison to encourage further research into the possibility that seismic anisotropy within different regions in the inner core could be explained by different phases of iron.

Anisotropic phases of iron, by themselves, do not account for the observed pattern of inner core anisotropy. The crystals must be aligned in a lattice preferred orientation (LPO) or alternatively in a shape preferred orientation (SPO), as a texture of randomly oriented anisotropic crystals would appear isotropic overall. Given a particular phase of iron, the question arises how this LPO is generated, and which mechanism(s) result in a heterogeneous distribution of this LPO. LPOs are commonly caused by post-solidification deformation, for the inner core one possible deformation mechanism would involve induced stresses causing axis symmetric flow, resulting in iron crystals aligning with this flow. A number of mechanisms have been proposed to create such texturing, including topographic relaxation (also known as equatorial growth, Yoshida et al. (1996)), whereby preferential growth at the equator of the inner core causes flow toward the poles due to geostatic forces. An alternative mechanism involves Maxwell stress or Lorentz forces induced by the magnetic field, causing deformation strongly influenced by outer core flow (Karato 1999; Buffett and Wenk 2001). It is likely that a combination of these mechanisms is required to explain the observed seismic complexity. For example, models of topographic relaxation typically produce symmetric flow around the equator which would create seismic anisotropy at

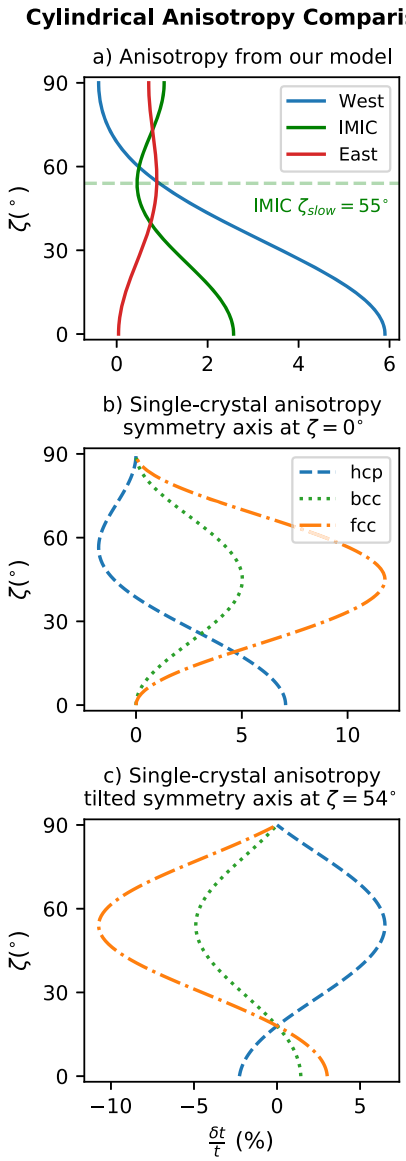

Fig. 9. a) Cylindrical anisotropy curves from three characteristic locations in our model. The western region represents the velocity variations from location: 90°W, 0°N, 800 km radius. The IMIC curve is from the location: 90°E, 45°N, 100 km radius. The eastern hemisphere curve is from the location: 90°E, 0°N at the inner core boundary. The horizontal green dashed line highlights the ζ_{slow} direction for the IMIC location. b) and c) show predicted single crystal anisotropy for three different iron crystal arrangements. b) shows the velocity variations of hcp, bcc, and fcc iron phases relative to velocity at $\zeta = 0^\circ$ assuming the c-axis of the hcp crystal is at $\zeta = 0^\circ$. c) shows the prediction if we consider the azimuth of maximum velocity through a single bcc or fcc crystal is at $\zeta = 54^\circ$. Values for the stiffness matrix for hcp and fcc iron are taken from Martorell et al. (2015) at 6600 K and at 360 GPa, while the values of the stiffness matrix for bcc iron was taken from Vočadlo (2007) at 6000 K. See Appendix B.5 for details on how to calculate predicted travel times from the stiffness matrix of a specific iron crystal.

both poles. This is in contrast to our observation that anisotropy in the inner core does not extend from south pole to north pole. Given this new observation, it is important that future geodynamical models assess whether topographic relaxation mechanisms can produce asymmetric flow around the equator, resulting in stronger anisotropy at the north pole than the south pole.

Hemispherical structures in the inner core are equally complicated to account for, and must further be compatible with the processes to generate anisotropy. Proposed hemispherical models are separated broadly based on whether the density or thermal profile in the inner core is stable. If the inner core has an unstable density or thermal profile, then convection becomes probable (Lythgoe and Deuss, 2015). For specific conditions (large viscosity and low thermal conductivity), this convection will be in the form of inner core translation which can result in a hemispherical pattern (Alboussiere et al. 2010; Deguen et al. 2018). An anisotropic fabric will be able to form if this translation is combined with a texturing mechanism such as topographical relaxation (Yoshida et al. 1996; Deguen et al. 2011), deformation due to magnetic forces (Karato, 1999) or annealing during translation (Bergman et al., 2010). For example, recent work by Frost et al. (2021) has shown that translation in the inner core is able to produce a region in the west with strong anisotropy. However, translation models require a high inner core viscosity ($> 10^{18}$ Pa s), which is not in agreement with current viscosity estimates of $10^{13} - 10^{17}$ (Koot and Dumberry, 2011; Ritterbex and Tsuchiya, 2020).

Alternatively, variations in crystallisation rate at the inner core boundary could result in hemispherical differences being 'frozen in' as the inner core grows (Aubert et al., 2008). In this case, heat flux at the ICB would be influenced by flow in the outer core, the magnetic field, and potentially thermal anomalies at the core mantle boundary (Karato 1993). This mechanism of hemisphere formation implies that structures at increasing depth within the inner core record older properties of ICB properties, outer core flow, and magnetic field strength. This opens the potential to use seismology to infer paleomagnetic properties, but it is also unclear if anomalies in the outer core could last long enough to maintain a consistent pattern of crystallisation in the inner core, and whether this pattern could truly be preserved for substantial periods of time.

8. Conclusion

Our transdimensional-MCMC model of inner core seismic velocity shows that hemispherical structures and regional-scale variations in anisotropy are required to explain inner core body wave data. The observed features remain when removing anomalous data from earthquakes originating in the South Sandwich Islands, and also when using data corrected for 3D mantle structure. Our results reveal for the first time that the strong anisotropic region in the west is primarily located in the northern hemisphere, with implications for geodynamical models of inner core formation. This result is guided only by the data itself without any prior structure imposed in the parameterisation, and is robust even when considering uncertainties in the data and model space. We propose to call this an anisotropic *zone* (rather than hemisphere) to better describe its shape. We also find robust evidence for a innermost inner core, in which the slowest velocity is at an angle of $55^\circ \pm 16$. The IMIC is offset by 400 km from the centre of the inner core and is contained mainly within the eastern hemisphere. Its distinct anisotropy could indicate a different phase of iron (either bcc or fcc) than the rest of the inner core (hcp), and potentially result from multiple stages of inner core growth, while its offset is compatible with models of slow lateral translation.

CRediT authorship contribution statement

Henry Brett: Conceptualization, Data curation, Formal analysis, Investigation, Methodology, Software, Writing – original draft. **Rhys Hawkins:** Methodology, Supervision, Writing – review & editing. **Lauren Waszek:** Data curation, Writing – review & editing. **Karen Lythgoe:** Data curation, Writing – review & editing. **Arwen Deuss:** Conceptualization, Funding acquisition, Project administration, Supervision, Writing – review & editing.

Declaration of competing interest

The authors declare that they have no known competing financial interests or personal relationships that could have appeared to influence the work reported in this paper.

Acknowledgements

This research was supported by the European Research Council (ERC) under the European Union's Horizon 2020 research and innovation programme (grant agreement No. 681535 - ATUNE) and a Vici award number 016.160.310/526 from the Netherlands Organisation for Scientific Research (NWO). LW acknowledges support from a Discovery Early Career Research Award (project number DE170100329), funded by the Australian Government. We thank the International Federation of Digital Seismograph Networks (FDSN) who stored and provided the data. Data processing was done using the Obspy and Scipy python packages while the code to conduct the inversion was written in the Julia programming language using multiple external libraries, the most important being 'QHULL' written by Barber, C.B, Dobkin, D.P., and Huhdanpaa, H.T.

Appendix. Supplementary material

Supplementary material related to this article can be found online at https://doi.org/10.1016/j.epsl.2022.117688.

References

Alboussiere, T., Deguen, R., Melzani, M., 2010. Melting-induced stratification above the Earth's inner core due to convective translation. Nature 466, 744–747.
Amaru, M.L., 2007. Global travel time tomography with 3-D reference models. Ph.D. thesis. Utrecht University. http://www.igitur.nl/.
Aubert, J., Amit, H., Hulot, G., Olson, P., 2008. Thermochemical flows couple the Earth's inner core growth to mantle heterogeneity. Nature 454, 758–761.
Beghein, C., Trampert, J., 2003. Robust normal mode constraints on inner-core anisotropy from model space search. Science 299, 552–555.
Bergman, M.I., Lewis, D.J., Myint, I.H., Slivka, L., Karato, S.I., Abreu, A., 2010. Grain growth and loss of texture during annealing of alloys, and the translation of Earth's inner core. Geophys. Res. Lett. 37.
Blom, N.A., Deuss, A., Paulssen, H., Waszek, L., 2015. Inner core structure behind the PKP core phase triplication. Geophys. J. Int. 201, 1657–1665.
Bodin, T., Sambridge, M., 2009. Seismic tomography with the reversible jump algorithm. Geophys. J. Int. 178, 1411–1436.
Brett, H., Deuss, A., 2020. Inner core anisotropy measured using new ultra-polar PKIKP paths. Geophys. J. Int.
Buffett, B., Wenk, H.R., 2001. Texturing of the Earth's inner core by Maxwell stresses. Nature 413, 60–63.
Burdick, S., Waszek, L., Lekić, V., 2019. Seismic tomography of the uppermost inner core. Earth Planet. Sci. Lett. 528, 115789.
Cowles, M.K., Carlin, B.P., 1996. Markov chain Monte Carlo convergence diagnostics: a comparative review. J. Am. Stat. Assoc. 91, 883–904.
Creager, K.C., 1992. Anisotropy of the inner core from differential travel times of the phases PKP and PKIKP. Nature 356, 309–314.
Crotwell, H.P., Owens, T.J., Ritsema, J., 1999. The TauP Toolkit: flexible seismic travel-time and ray-path utilities. Seismol. Res. Lett. 70, 154–160.
Deguen, R., Alboussière, T., Labrosse, S., 2018. Double-diffusive translation of Earth's inner core. Geophys. J. Int. 214, 88–107.
Deguen, R., Cardin, P., Merkel, S., Lebensohn, R.A., 2011. Texturing in Earth's inner core due to preferential growth in its equatorial belt. Phys. Earth Planet. Inter. 188, 173–184.
Dziewonski, A.M., Gilbert, F., 1976. The effect of small, aspherical perturbations on travel times and a re-examination of the corrections for ellipticity. Geophys. J. Int. 44, 7–17.
Frost, D.A., Lasbleis, M., Chandler, B., Romanowicz, B., 2021. Dynamic history of the inner core constrained by seismic anisotropy. Nat. Geosci., 1–5.
Frost, D.A., Romanowicz, B., 2019. On the orientation of the fast and slow directions of anisotropy in the deep inner core. Phys. Earth Planet. Inter. 286, 101–110.
Frost, D.A., Romanowicz, B., Roecker, S., 2020. Upper mantle slab under Alaska: contribution to anomalous core-phase observations on South-Sandwich to Alaska paths. Phys. Earth Planet. Inter. 106427.
Hastings, W.K., 1970. Monte Carlo sampling methods using Markov chains and their applications.
Irving, J.C.E., Deuss, A., 2011. Hemispherical structure in inner core velocity anisotropy. J. Geophys. Res., Solid Earth 116.
Ishii, M., Dziewoński, A.M., 2003. Distinct seismic anisotropy at the centre of the Earth. Phys. Earth Planet. Inter. 140, 203–217.
Karato, S.I., 1993. Inner core anisotropy due to the magnetic field—induced preferred orientation of iron. Science 262, 1708–1711.
Karato, S.I., 1999. Seismic anisotropy of the Earth's inner core resulting from flow induced by Maxwell stresses. Nature 402, 871–873.
Kennett, B., Engdahl, E., Buland, R., 1995. Constraints on seismic velocities in the Earth from traveltimes. Geophys. J. Int. 122, 108–124.
Koot, L., Dumberry, M., 2011. Viscosity of the Earth's inner core: constraints from nutation observations. Earth Planet. Sci. Lett. 308, 343–349.
Lehmann, I., 1936. P'. Publ. Bur. Centr. Seism. Internat. Serie A 14, 87–115.
Li, C., van der Hilst, R.D., Engdahl, E.R., Burdick, S., 2008. A new global model for P wave speed variations in Earth's mantle. Geochem. Geophys. Geosyst. 9.
Lythgoe, K., Deuss, A., Rudge, J., Neufeld, J., 2014. Earth's inner core: innermost inner core or hemispherical variations? Earth Planet. Sci. Lett. 385, 181–189.
Lythgoe, K.H., Deuss, A., 2015. The existence of radial anisotropy in Earth's upper inner core revealed from seismic normal mode observations. Geophys. Res. Lett. 42, 4841–4848.
Martorell, B., Brodholt, J., Wood, I.G., Vočadlo, L., 2015. The elastic properties and stability of fcc-fe and fcc-feni alloys at inner-core conditions. Geophys. J. Int. 202, 94–101.
Morelli, A., Dziewonski, A.M., Woodhouse, J.H., 1986. Anisotropy of the inner core inferred from PKIKP travel times. Geophys. Res. Lett. 13, 1545–1548.
Niu, F., Wen, L., 2001. Hemispherical variations in seismic velocity at the top of the Earth's inner core. Nature 410, 1081–1084.
Panning, M., Romanowicz, B., 2006. A three-dimensional radially anisotropic model of shear velocity in the whole mantle. Geophys. J. Int. 167, 361–379.
Pejić, T., Hawkins, R., Sambridge, M., Tkalčić, H., 2019. Transdimensional bayesian attenuation tomography of the upper inner core. J. Geophys. Res., Solid Earth 124, 1929–1943.
Ritterbex, S., Tsuchiya, T., 2020. Viscosity of hcp iron at Earth's inner core conditions from density functional theory. Sci. Rep. 10, 1–9.
Simmons, N.A., Myers, S.C., Johannesson, G., Matzel, E., 2012. LLNL-G3Dv3: global P wave tomography model for improved regional and teleseismic travel time prediction. J. Geophys. Res., Solid Earth 117.
Stephenson, J., Tkalčić, H., Sambridge, M., 2020. Evidence for the innermost inner core: robust parameter search for radially varying anisotropy using the neighbourhood algorithm. J. Geophys. Res., Solid Earth e2020JB020545.
Sun, X., Song, X., 2008a. The inner inner core of the Earth: texturing of iron crystals from three-dimensional seismic anisotropy. Earth Planet. Sci. Lett. 269, 56–65.
Sun, X., Song, X., 2008b. Tomographic inversion for three-dimensional anisotropy of Earth's inner core. Phys. Earth Planet. Inter. 167, 53–70.
Tanaka, S., Hamaguchi, H., 1997. Degree one heterogeneity and hemispherical variation of anisotropy in the inner core from PKP (BC)-PKP (DF) times. J. Geophys. Res., Solid Earth 102, 2925–2938.
Tesoniero, A., Auer, L., Boschi, L., Cammarano, F., 2015. Spani, a whole-mantle Vp and Vs model: implications on thermo-chemical structure. EGUGA 10514.
Tkalčić, H., 2010. Large variations in travel times of mantle-sensitive seismic waves from the South Sandwich Islands: is the Earth's inner core a conglomerate of anisotropic domains? Geophys. Res. Lett. 37.
Vočadlo, L., 2007. Ab initio calculations of the elasticity of iron and iron alloys at inner core conditions: evidence for a partially molten inner core? Earth Planet. Sci. Lett. 254, 227–232.
Waszek, L., Deuss, A., 2011. Distinct layering in the hemispherical seismic velocity structure of Earth's upper inner core. J. Geophys. Res., Solid Earth 116.
Wen, L., Niu, F., 2002. Seismic velocity and attenuation structures in the top of the Earth's inner core. J. Geophys. Res., Solid Earth 107, ESE-2.
Woodhouse, J.H., Giardini, D., Li, X.D., 1986. Evidence for inner core anisotropy from free oscillations. Geophys. Res. Lett. 13, 1549–1552.
Yoshida, S., Sumita, I., Kumazawa, M., 1996. Growth model of the inner core coupled with the outer core dynamics and the resulting elastic anisotropy. J. Geophys. Res., Solid Earth 101, 28085–28103.